One-dimensional compression of a saturated elastoviscoplastic medium

Daniel T. Paterson,[1] Tom S. Eaves,[2] Duncan R. Hewitt,[3] Neil J. Balmforth,[4] and D. Mark Martinez[1]

[1]*Department of Chemical and Biological Engineering, University of British Columbia, Vancouver, British Columbia V6T 1Z4, Canada*

[2]*School of Science and Engineering, University of Dundee, Fulton Building, Dundee DD1 4HN, United Kingdom*

[3]*Department of Mathematics, University College London, London WC1H 0AY, United Kingdom*

[4]*Department of Mathematics, University of British Columbia, Vancouver, British Columbia V6T 1Z2, Canada*

(Received 20 January 2022; accepted 9 May 2022; published 31 May 2022)

A theoretical and experimental study is presented of the one-dimensional compression of a networked suspension. Particular attention is given to relatively rapid compression where we extend previous works by including an elastoviscoplastic constitutive relation. Solutions of a one-dimensional model are presented, and asymptotic limits explored, for compressions controlling either displacement or load. The results are compared to complementary laboratory experiments using cellulose fiber suspensions, with the material functions appearing in the model calibrated by independent experiments. Measurements of load and local solid velocity as a function of displacement during compression and unloading gauge the importance of elastic effects. The comparison between experiment and theory is satisfying, demonstrating a dramatic improvement over existing inelastic constitutive models in reproducing the observed differential spatial compaction.

DOI: 10.1103/PhysRevFluids.7.054303

I. INTRODUCTION

The consolidation of a saturated porous material features in a great many problems in geophysics and engineering, ranging from the compaction of soils to industrial filtration and the dewatering of suspensions. Models for these problems are often founded on two-phase flow theory, with Darcy's law describing the fluid flow through the collapsing solid and the stress decomposed by Terzaghi's principle into the fluid pore pressure and an effective solid stress. In the classical theory of poroelasticity (e.g., [1–3]), the effective stress is assumed to originate from the elastic response of the solid matrix. For suspensions, this stress is more commonly assumed to reflect plastic rearrangements or deformations of the interconnected solid particles [4–7]. Either way, a simple constitutive description follows from prescribing the effective stress in terms of the local solid volume fraction, and whether this stress has an elastic or plastic origin becomes largely irrelevant.

Despite this classical approach, there is no special reason for assuming that the effective stress is a function of purely the solid fraction, other than one of expedience. Indeed, the compaction of suspensions can show distinctive rate dependence and hysteresis during cycles of loading and unloading [8–15], demanding a richer constitutive description. For example, for suspensions of cellulose fibers or saturated paper sheets, it is commonly assumed that plastic rearrangements of the cellulose matrix give rise to network strength. Nevertheless, in the dewatering of suspensions

of cellulose fibers or the swelling of paper under capillary imbibition, it has been found that the solid stress must be rate-dependent in order to reconcile theoretical models with experimental observations [15–19]. There is also much evidence from the industrial processing of pulp and paper that elastic stresses can play an important role in suspensions of cellulose fibers [10,11,20–22]. Similar contributions from plastic, elastic, and viscous stresses feature in the deformation of soils and thick pastes (e.g., [23]).

Such considerations motivate the current paper: we introduce and explore a simple model for the consolidation of a two-phase material, allowing for an elastoviscoplastic solid stress. Such an approach is not new, with developments in plasticity theory already extended to two-phase formulations (e.g., [1]). By building on the framework of nonlinear elasticity, however, and in particular accommodating finite three-dimensional strains, the constitutive description becomes somewhat daunting and lacks transparency. For the present task, we are inspired by constitutive models for single-phase complex fluids that mix plasticity with viscoelasticity, or equivalently, elasticity with viscoplasticity. More specifically, as a prescription for the stress in the solid phase, we employ a particular model formulated by Saramito [24] that adds a plastic yield stress to the Maxwell model of a viscoelastic fluid (in one spatial dimension; for higher dimensions the yield stress is added to an Oldroyd B model). This description has the advantage of simplicity and transparency: the associated material parameters or functions can be calibrated with simple experiments, and idealized consolidation problems can be studied with only modest effort. An important assumption is that the chief price that must be paid by using this description is one of quantitative accuracy, and no critical physical effects are omitted.

With the constitutive model in hand, and incorporated into a two-phase formulation, we explore an idealized one-dimensional consolidation problem; the familiar "coffee press" configuration. With a solid stress that depends purely on solid fraction ϕ, the mathematical formulation of this problem boils down to a nonlinear diffusion equation for ϕ that can be solved for compressions at either fixed rate or prescribed load (e.g., [2,25–29]). The impact of adding to this model a rate-dependent solid stress with the form of a simple bulk viscosity was considered in [15]; earlier models incorporating viscoelastic constitutive laws were presented by [9,30–33]. Our goal here is to consider the elastoviscoplastic version of the problem, providing a theoretical discussion complemented by experiments with suspensions of cellulose fibers. Importantly, we proceed beyond the dynamics of compression at constant speed or load, allowing the press to slow, stop, and even unload, all of which can potentially set the stage for differentiating plastic deformations from elastic ones.

II. CONSTITUTIVE MODEL

A. Statement of the model

To describe the constitutive behavior under one-dimensional compression, we assume that solid stress originates purely from elastic deformation provided it does not exceed a critical stress. Once that threshold is exceeded, the solid also deforms plastically. For a spatially uniform medium, the solid effective (compressive) stress $\hat{\mathcal{P}}$ satisfies

$$\frac{1}{\mathcal{E}(\phi)}\frac{d\hat{\mathcal{P}}}{d\hat{t}} + \frac{1}{\hat{\Lambda}(\phi)}\max\left(0, \frac{|\hat{\mathcal{P}}| - P_Y(\phi)}{|\hat{\mathcal{P}}|}\right)\hat{\mathcal{P}} = -\dot{e}, \tag{1}$$

where the compression (strain) rate is

$$\dot{e} \equiv -\frac{1}{\phi}\frac{d\phi}{dt} \tag{2}$$

($-\log\phi$ being the one-dimensional logarithmic or Hencky strain). The constitutive relation Eq. (1) incorporates a yield condition at $|\hat{\mathcal{P}}| = P_Y(\phi)$, below which the stress satisfies the elastic law, $d\hat{\mathcal{P}}/dt = -\mathcal{E}\dot{e}$ with bulk modulus $\mathcal{E}(\phi)$. Above the yield condition, for $|\hat{\mathcal{P}}| > P_Y$, deformation

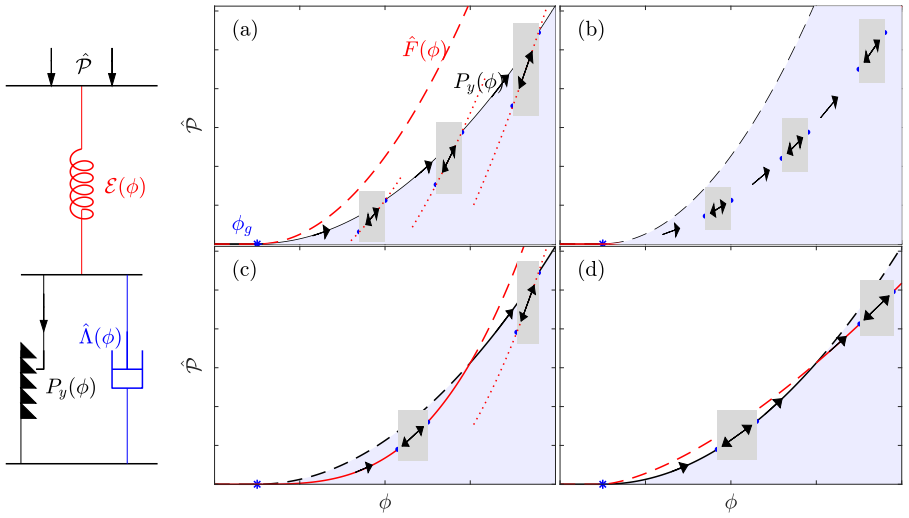

FIG. 1. Sketches showing the constitution of each material element in our model elastoviscoplastic medium (left), and the four simplest types of quasistatic compression dynamics (right; (a)–(d). On the right, the light blue shading indicates when the material has yielded, the black (solid or dashed) lines show $P_Y(\phi)$, and the red (solid or dashed) lines indicate $\hat{F}(\phi)$. Quasistatic compression follows either $P_Y(\phi)$ or $\hat{F}(\phi)$ depending on their relative magnitudes; the sections of these curves that are followed are drawn by solid lines (and are dashed otherwise). The gray-shaded rectangles illustrate the response when compression is interrupted by a cycle of limited unloading and reloading. If this response is elastic, but begins from a point on the compressive yield stress curve, the unloading-reloading follows a translated elastic curve $\hat{F}(\phi) + \text{const}$ indicated by the red dotted lines.

occurs with a bulk viscosity $\hat{\Lambda}(\phi)$. The compressive, plastic yield stress is $P_Y(\phi)$. The model in Eq. (1) has become popular in non-Newtonian fluid mechanics to describe single-phase elastoviscoplastic liquids, although here we take the material parameters to all be functions of the local solid fraction. Pictorially, the model can be characterized as placing an elastic spring in series with a ratchet and dashpot paired in parallel, for each material element in the medium; see Fig. 1.

When $\mathcal{E} \to \infty$, elastic effects disappear from Eq. (1) to leave the viscoplastic law $\hat{\mathcal{P}} = -P_Y(\phi)\,\mathrm{sgn}(\dot{\epsilon}) - \hat{\Lambda}\dot{\epsilon}$ for $|\hat{\mathcal{P}}| > P_Y$. If, in addition, the bulk viscosity is negligible ($\hat{\Lambda} \to 0$), we finally arrive at the consolidation law $\hat{\mathcal{P}} = -P_Y(\phi)\,\mathrm{sgn}(\dot{\epsilon})$ used both in soil mechanics (e.g., [2,34]) and for colloidal suspensions (e.g., [4,27]).

The purely elastic part of the law, applying below the yield stress, is equivalent to the prescription

$$\frac{d}{dt}[\hat{\mathcal{P}} - \hat{F}(\phi)] = 0, \quad \hat{F}(\phi) \equiv \int^{\phi} \check{\phi}^{-1}\mathcal{E}(\check{\phi})\,d\check{\phi}. \tag{3}$$

That is, the effective stress is a prescribed function of the solid fraction, in the usual manner of Biot's theory of poroelasticity. As commented in Sec. I, this leads to a solid stress model that is superficially similar to the simple consolidation law $\hat{\mathcal{P}} = -P_Y(\phi)\,\mathrm{sgn}(\dot{\epsilon})$. However, the factor $\mathrm{sgn}(-\dot{\epsilon})$ incorporates the yield-stress hysteresis into the plastic model in place of elastic reversibility.

B. Quasistatic loading and unloading

To gain a first insight into the constitutive behavior captured by the model, we first consider its predictions when compression takes place quasistatically. In this limit, the model displays different behavior depending on the relative magnitudes of the compressive yield stress $P_Y(\phi)$ and the elastic

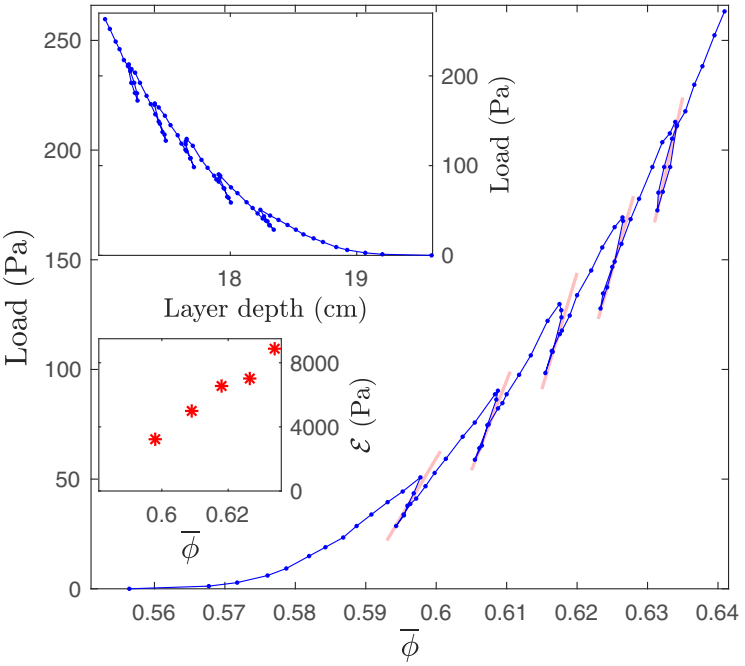

FIG. 2. Compression curves interrupted by limited unloading-reloading cycles for a hydrogel suspension. The short red lines indicate local fits to each unloading-reloading section. The insets show the original piston position vs load data, and the values for $\mathcal{E}(\phi)$ extracted from the loading-reloading fits.

stress function $\hat{F}(\phi)$ in Eq. (3), as illustrated in Fig. 1. If $P_Y < \hat{F}$, deformation is plastic with the solid stress following P_Y [Fig. 1(a)]. For $P_Y > \hat{F}$, on the other hand, the material deforms elastically and $\hat{\mathcal{P}} = \hat{F}$ [Fig. 1(b)]. The elastic-plastic behavior seen in Fig. 1(a) is familiar from the testing of soils (e.g., Refs. [1,2,34]) and slurries [9]. Note that in the illustrative plots we have assumed that the solid matrix establishes only a network that can resist stress beyond some gel point, $\phi = \phi_g$ (i.e., $P_Y = \hat{F} = 0$ for $\phi \leqslant \phi_g$).

Because the material functions P_Y and $\hat{F}$ are solid-fraction-dependent, if their functional forms are different, the compressive yield stress curve can intersect the elastic stress function at a special solid fraction. Assuming that only one such intersection takes place, two further possibilities then emerge, as illustrated in Figs. 1(c) and 1(d). In these cases, the compression first follows the elastic curve before yielding and following the compressive yield stress [Fig. 1(c)] or vice versa [Fig. 1(d)].

Further implications of the constitutive law can be extracted by considering the result of interrupting the quasistatic compression by a limited cycle of unloading and reloading. What transpires during these cycles depends on whether the material has previously yielded or not. If $\hat{\mathcal{P}} = \hat{F}$ when compression is interrupted, the material elastically recovers and recompresses along the $\hat{F}$ curve during the cycle, as in Fig. 1(b) where the plastic yield stress is always too large to play any role in the mechanics of the material. If, however, $\hat{\mathcal{P}} = P_Y$, the material immediately becomes unyielded at the moment that unloading begins and deforms elastically until the cycle ends. The stress during the cycle cannot follow the original $\hat{F}$ curve, however, because an amount of unrecoverable plastic strain has occurred along the compressive yield stress curve. Instead, as indicated by the integral of Eq. (3), the relevant stress pathway is a translated curve, $\hat{\mathcal{P}} = \hat{F} + \text{const}$, that intersects the P_Y curve at the point where unloading begins [see Figs. 1(a) and 1(c)]. Note, however, that in regions where $\hat{\mathcal{P}} = P_Y$ but $\partial P_Y/\partial\phi > \partial\hat{F}/\partial\phi$, as in the lower shaded region in Fig. 1(d), the material cannot recover along the elastic curve, because in doing so it would be raised above the yield stress; in

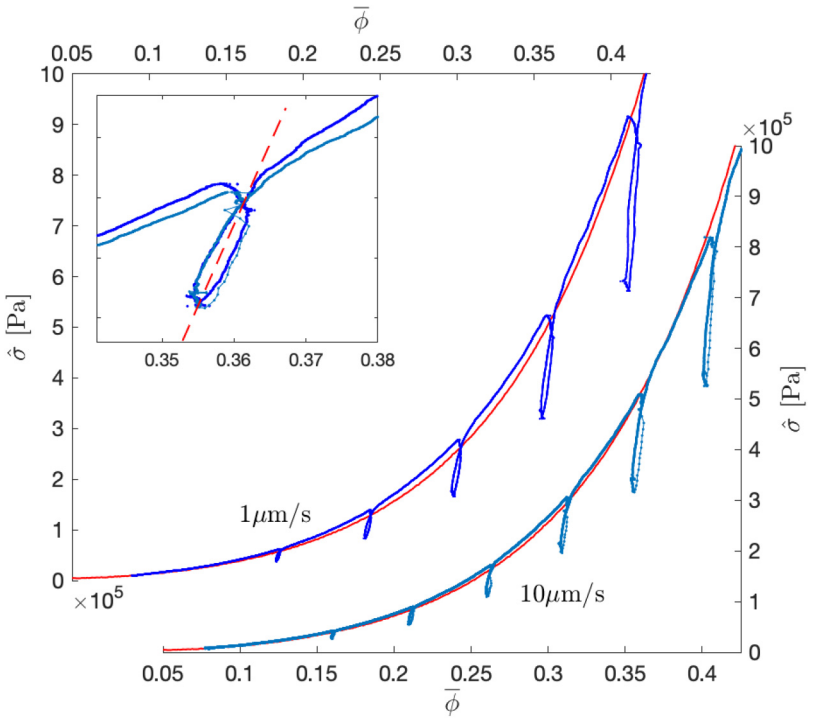

FIG. 3. Compression curves interrupted by limited unloading-reloading cycles for a suspension of cellulose fibers. Two tests are shown, conducted at compression rates of 1 μm/s; in the first test, the unloading rate is the same, but in the second it is increased to 10 μm/s. The red line shows the pure compression test calibrating $P_Y(\phi)$. The inset shows a detail of one of the cycles, together with the fit giving $\mathcal{E}(\phi)$.

this case, the elastic stresses must instead drive plastic deformation, and the response follows the P_Y curve as shown in the figure.

As implied by the comparisons with experimental observations reported next, we will be most concerned with a medium with the behavior shown in Fig. 1(a); i.e., a medium with $P_Y < \hat{F}$, for which unloadings depart from the compressive stress curve along steeper elastic contours under quasistatic conditions. This type of solid matrix may well describe a suspension in which the constituent particles can move relative to one another to consolidate, which is resisted by frictional forces stemming from somewhat larger normal forces due to Hertzian contact or elastic bending and collapse.

C. Experimental support

The predictions of the constitutive model for quasistatic loadings interrupted by limited cycles of unloading and reloading reproduce observations taken from experiments with suspensions of hydrogel or cellulose fibers. The first of these experiments consisted of a relatively crude apparatus in which a 20-cm-deep settled suspension of hydrogel spheres of radius 9 mm was compressed in a box by a plunger. The box had a 16 cm $\times$ 16 cm square cross section; the plunger was slightly smaller, enabling water to freely pass around the sides while trapping the spheres underneath. The plunger was fixed to a milling table and its position adjusted in a series of steps with a screw. The load after each step was measured by placing a scale underneath the box. The depth of the hydrogel layer was measured by taking photographs from the side and processing the images. In the second experiment, the specially designed compression device reported in [15,18] was used with

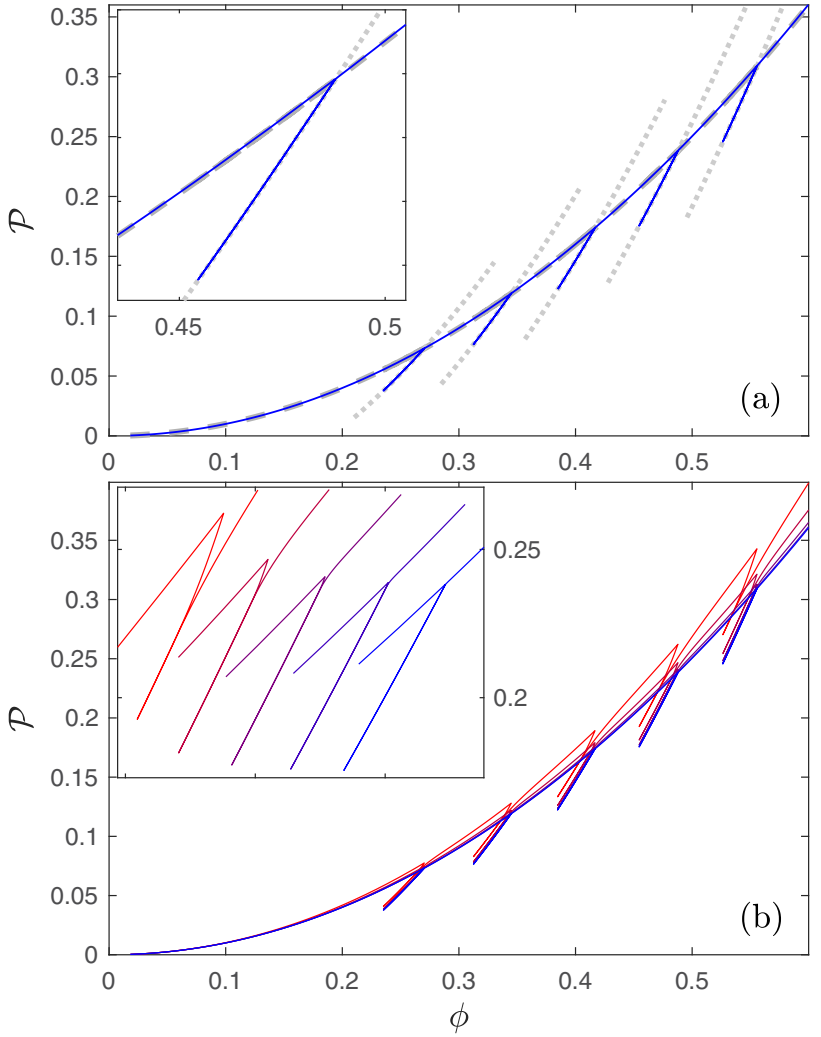

FIG. 4. Compression curves interrupted by limited unloading-reloading cycles for the model Eq. (1) with $(\mathcal{E}, \hat{\Lambda}, P_Y) = (\mathcal{E}_*, \eta_*, p_*)\phi^2$. In (a) scaled stress $\mathcal{P} = \hat{P}/p_*$ (blue curve) is plotted for $\epsilon/\gamma \equiv \eta_* U/(h_0 p_*) = 10$ and $\epsilon/(\gamma\lambda) \equiv \mathcal{E}_*/p_* = 4$, where U/h_0 is the compression rate (see Sec. III C) The black dashed and dotted lines display $\Pi_Y = P_Y/p_*$ and the translated $F = \hat{F}/p_*$ curves. For (b) we show solutions in which the compression rate is increased so that $\epsilon/\gamma \equiv \eta_* U/(h_0 p_*) = 10^{(j-2)/2}$ with $j = 0, 1, \ldots, 4$ (from blue to red). The insets show details of one of the cycles [with the different solutions successively offset horizontally by 0.04 in (b) for clarity].

suspensions of cellulose fibers. In this case, the plunger position is remotely controlled, following a preset compression sequence; more details of the cellulose fiber experiments appear below in Sec. VI. Figures 2 and 3 show sample results for tests in which cycles of limited unloading and reloading interrupted a net compression (plotting load $\hat{\sigma}$ against average solid fraction $\overline{\phi}$).

For comparison, Fig. 4(a) shows a complementary numerical solution of the model (1), with constitutive functions and parameters chosen as indicated in the caption. We ignore any gel point and set $\phi_g = 0$. Note that the model at this stage contains no differential compaction in space due to dynamic dewatering (which is introduced in the next section), allowing us to solve (1) directly for a spatially uniform material with no further dynamical considerations. The structure

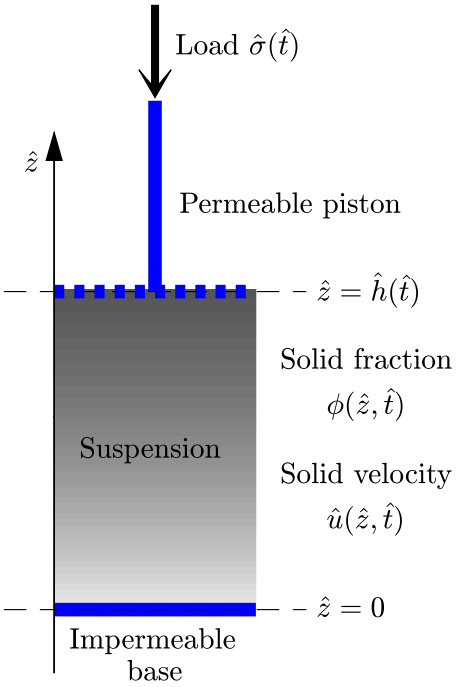

FIG. 5. A sketch of the two-phase model geometry.

of the interrupted compression curves is similar to that observed experimentally (for the sequence of main compression and limited unloading-reloading cycles adopted). The finer structure of the compression curves over the unloading-reloading cycles is a little different, however, with the observations suggesting that a loop can open up during the cycle. The theoretical compression curves, in contrast, do not show loops [Fig. 4(a)]. These curves become merely shifted off the P_Y and $\hat{F}$ lines when the compression is performed faster and we move away from the quasistatic limit; see Fig. 4(b), which presents further solutions to Eq. (1) with higher strain rates. This suggests that the loops in the experimental curves are not due to a finite compression rate. Indeed, conducting the test shown in Fig. 3 a second time, but with a faster unloading rate, leads to no obvious systematic change in the structure of the loops arising during the unloading-reloading cycles (see the inset to Fig. 3).

Note also that these interrupted compression curves can be employed to calibrate the functions $P_Y(\phi)$ and $\hat{F}(\phi)$ [or $\mathcal{E}(\phi)$]. In particular, the main loading sequence provides the compressive yield stress, whereas the interruptions furnish the local elastic bulk modulus at the initiation of unloading [the local slope here is $\partial\hat{F}/\partial\phi = \phi^{-1}\mathcal{E}(\phi)$], as illustrated in Fig. 2 and the inset to Fig. 3.

III. DYNAMIC DEWATERING MODEL

A. Mathematical formulation

Moving on to the dynamics of compression, we now consider a one-dimensional, two-phase medium in which fluid flows through a solid matrix that collapses under the action of a load $\hat{\sigma}(\hat{t})$ imposed by a permeable piston. Each phase is incompressible, with constant solid and fluid densities. As sketched in Fig. 5, we denote position and time by $\hat{z}$ and $\hat{t}$. The piston, which retains all the solid beneath, has position $\hat{z} = \hat{h}(\hat{t})$, and there is an impermeable base at $\hat{z} = 0$. The differential compaction of the solid is described by the local volume fraction, $\phi(\hat{z}, \hat{t})$ and solid velocity $u(\hat{z}, \hat{t})$;

initially, the solid matrix is uniform and motionless with $\phi(\hat{z},0)=\phi_0$. The velocity of the fluid is $\hat{v}(\hat{z},\hat{t})$.

Replacing the ordinary time derivatives with material derivatives following the local solid motion (cf. [28,34]), the constitutive law becomes

$$\frac{1}{\mathcal{E}}\frac{D\hat{\mathcal{P}}}{D\hat{t}}+\frac{1}{\hat{\Lambda}}\max\left(0,\frac{|\hat{\mathcal{P}}|-P_y}{|\hat{\mathcal{P}}|}\right)\hat{\mathcal{P}}=\frac{1}{\phi}\frac{D\phi}{D\hat{t}}, \tag{4}$$

where

$$\frac{D}{D\hat{t}}\equiv\frac{\partial}{\partial\hat{t}}+\hat{u}\frac{\partial}{\partial\hat{z}}. \tag{5}$$

We embed this relation in a two-phase formulation by adopting Terzaghi's principle and assuming that inertia and gravity are negligible. Conservation of mass, Darcy's law, and force balance then demand that

$$\frac{\partial\phi}{\partial\hat{t}}+\frac{\partial}{\partial\hat{z}}(\phi\hat{u})=0, \tag{6}$$

$$-\frac{\partial\phi}{\partial\hat{t}}+\frac{\partial}{\partial\hat{z}}[(1-\phi)\hat{v}]=0, \tag{7}$$

$$(1-\phi)(\hat{v}-\hat{u})=-\frac{k(\phi)}{\mu}\frac{\partial\hat{p}}{\partial\hat{z}}, \tag{8}$$

$$\frac{\partial}{\partial\hat{z}}(\hat{p}+\hat{\mathcal{P}})=0, \tag{9}$$

where $\hat{p}$ and μ are the fluid pore pressure and viscosity, respectively, and $k(\phi)$ is the permeability.

At the impermeable base $\hat{z}=0$, we impose $\hat{u}(0,\hat{t})=\hat{v}(0,\hat{t})=0$. A combination of (6) and (7) yields the bulk continuity equation, which integrates to

$$\phi\hat{u}+(1-\phi)\hat{v}=0,$$

demanding that the fluid velocity is $\hat{v}=-\phi\hat{u}/(1-\phi)$. The Darcy flux is therefore $(1-\phi)(\hat{v}-\hat{u})=-\hat{u}$, which can be introduced into Darcy's law to remove the fluid velocity from Eqs. (6), (8), and (9) and render Eq. (7) redundant.

At $z=\hat{h}(\hat{t})$, we demand

$$\hat{u}(\hat{h},\hat{t})=\frac{d\hat{h}}{d\hat{t}},\quad \hat{p}(\hat{h},\hat{t})=0,\quad \hat{\mathcal{P}}(\hat{h},\hat{t})=\hat{\sigma}(\hat{t}), \tag{10}$$

neglecting any flow resistance through the piston and ignoring air pressure.

The choice of the material derivative in Eq. (5) deserves some comment, as the effective stress may not be convected with the solid velocity. Indeed, Preziosi *et al.* [32] employ the mass-average velocity,

$$u_m=\frac{\phi\rho_s\hat{u}+(1-\phi)\rho_f\hat{v}}{\phi\rho_s+(1-\phi)\rho_f}\equiv\frac{\phi(\rho_s-\rho_f)\hat{u}}{\phi\rho_s+(1-\phi)\rho_f},$$

to convect $\hat{\mathcal{P}}$ in their formulation for a viscoelastic effective stress, where ρ_s and ρ_f denote the fluid and solid densities. For the current problem, this choice would allow no convection if there was no density difference between the two phases. Moreover, in order that the model recover the elastic limit described in Sec. III D, the material derivative in Eq. (5) must match that implied by Eq. (6). For these reasons, and in the interest of retaining a simple model formulation, we therefore persist with Eq. (5). An alternative would be to replace $\hat{u}$ by $c(\phi)\hat{u}$ in this derivative, at the expense of the burden of a further material function $c(\phi)$ [given that $\hat{v}=-\phi\hat{u}(1-\phi)^{-1}$, which implies that all linear combinations of the velocities of the two phases take this form].

B. Material functions

To close the system of equations, material functions are needed to set the dependence of the permeability $k(\phi)$ on the solid fraction and dictate the coefficients of the constitutive law. For the permeability law, when exploring the dynamics captured by the model, we adopt the simple power law

$$k(\phi) = k_* \phi^{-a}, \tag{11}$$

where a is a parameter and k_* represents a characteristic permeability scale. Later, when comparing theoretical results with experiments using a particular porous medium (a suspension of cellulose fibers), we employ a more complicated, but experimentally calibrated, permeability function.

The elastoviscoplastic law requires three more material functions: for these, we take for illustration

$$P_y(\phi) = p_* \phi^n, \quad \mathcal{E}(\phi) = \mathcal{E}_* \phi^m \quad \text{and} \quad \hat{\Lambda} = \eta_* \phi^2, \tag{12}$$

where $(p_*, \mathcal{E}_*, \eta_*)$ are again characteristic scales and n and m are parameters. Again, we will later employ richer forms for $P_y(\phi)$ and $\mathcal{E}(\phi)$ guided by calibration experiments for cellulose suspensions. The bulk viscosity is more difficult to constrain empirically; in the interest of simplicity, and in view of previous successes for pulp, we continue with the power-law form for $\hat{\Lambda}(\phi)$ in (12).

C. Dimensionless model equations

We remove dimensions from the model equations using the scalings

$$(\hat{z}, \hat{h}) = h_0(z, h), \quad \hat{u} = U u, \quad \hat{t} = \frac{h_0}{U} t, \quad \text{and} \quad \hat{\mathcal{P}} = p_* \mathcal{P}, \tag{13}$$

where h_0 represents the initial height of the suspension, and U is the initial compression speed. Then

$$\frac{D\phi}{Dt} = -\phi \frac{\partial u}{\partial z}, \tag{14}$$

$$u = -\gamma K(\phi) \frac{\partial \mathcal{P}}{\partial z}, \tag{15}$$

$$\frac{\lambda \Lambda(\phi)}{E(\phi)} \frac{D\mathcal{P}}{Dt} = -\frac{\epsilon}{\gamma} \Lambda(\phi) \frac{\partial u}{\partial z} - \max\left(0, \frac{|\mathcal{P}| - \Pi_y(\phi)}{|\mathcal{P}|}\right) \mathcal{P}, \tag{16}$$

where

$$\gamma = \frac{p_* k_*}{\mu h_0 U}, \quad \epsilon = \frac{k_* \eta_*}{\mu h_0^2}, \quad \text{and} \quad \lambda = \frac{\eta_* U}{h_0 \mathcal{E}_*} \tag{17}$$

denote dimensionless groups dictating the rapidity of dewatering and the relative strengths of bulk viscosity and a Weissenberg number measuring the importance of elasticity. The dimensionless versions of the material constitutive functions are

$$K = \frac{k}{k_*}, \quad \Pi_y = \frac{P_y}{p_*}, \quad E = \frac{\mathcal{E}}{\mathcal{E}_*}, \quad \text{and} \quad \Lambda = \frac{\hat{\Lambda}}{\eta_*}. \tag{18}$$

The initial and boundary conditions are

$$\phi(z, 0) = \phi_0, \quad \mathcal{P}(0, t) = \Pi_y(\phi_0), \tag{19}$$

$$u(h, t) = \dot{h}(t), \quad \mathcal{P}(h, t) = \sigma(t), \tag{20}$$

where $\sigma(t) = \hat{\sigma}/p_*$ is the dimensionless stress on the piston and we assume that the material has been deformed plastically (by, for example, slow stirring) to arrange it into its initial state.

Two versions of the compaction problem posed above are possible. In an analog of the familiar "coffee press," one can control the position of the piston; $h(t)$ is then an input variable, and the load $\sigma(t)$, together with the solid distribution $\phi(z,t)$, is an output. Alternatively, for fixed load, one controls $\sigma(t)$ and the piston position and $\phi(z,t)$ are output.

D. Plastic and unyielded limits

If either $\lambda = \epsilon = 0$ or $|\mathcal{P}| < \Pi_y$ for all time, we recover the nonlinear diffusion equation,

$$\phi_t = [D(\phi)\phi_z]_z, \tag{21}$$

where

$$D(\phi) = \gamma\phi K(\phi) \times \begin{cases} \Pi_y'(\phi), & \lambda = \epsilon = 0 \\ F'(\phi), & |\mathcal{P}| < \Pi_y \end{cases} \tag{22}$$

(assuming that $D\phi/Dt > 0$, or $\mathcal{P} > 0$, for $\epsilon = \lambda = 0$),

$$F(\Phi) = \epsilon(\gamma\lambda)^{-1} \int \phi^{-1} E(\phi)\, d\phi \tag{23}$$

is the dimensionless version of the elastic stress function $\hat{F}(\phi)$, and the prime indicates differentiation with respect to ϕ. The nonlinear diffusion Eq. (21) corresponds to that used in previous work for purely plastic or elastic solid stresses.

More generally, where the material is unyielded, the model indicates that

$$\frac{D}{Dt}[\mathcal{P} - F(\phi)] = 0. \tag{24}$$

Hence, the solid stress is known only up to that left behind by the unrecoverable plastic strain arising prior to the yield point: $\mathcal{P} = \mathcal{P}_0(z_0, t_0) + F(\phi)$, where (z_0, t_0) denote the position and time where the local material element reached the yield stress and $\mathcal{P}_0(z_0, t_0) \equiv \Pi_y(\phi(z_0, t_0))$. In general, this embeds a history dependence into the solid stress that precludes any reduction to Eq. (21).

IV. INVESTIGATING THE MODEL

To study the dynamical dewatering behavior captured by the model, we first present solutions for some idealized fixed-rate and fixed-load compression problems. We use the idealized power-law material functions of Sec. III B, choosing $n = m$, and initialize with $\phi_0 = 0.05$. With fixed-rate compression, the characteristic speed U is specified; the parameter γ can then be thought of as gauging the rate of dewatering. For the fixed-load problem, on the other hand, the load on the piston is prescribed, leading us to set $\sigma = R$, where R is the ratio of the piston load to p_* (assumed greater than unity, so that the solid is forced to collapse). The characteristic piston speed is left unset; we then select this scale so that $\gamma = 1$. In either case, the remaining parameters from the constitutive law are ϵ and λ, measuring the importance of the bulk viscosity and elasticity, respectively.

A. Fixed-rate compression

We begin by reconsidering the interrupted compression sequences of Secs. II B and II C. Now, the descent of the permeable piston can differentially compact the solid to raise the load at the top above the compressive yield stress expected from the mean solid fraction $\overline{\phi}(t)$. In the absence of elastic effects and bulk viscosity, the solid compacts uniformly when the rate of dewatering is low (the parameter γ is large), as in Secs. II B and II C. But with more rapid dewatering ($\gamma \ll 1$), the solid builds up significantly against the piston while remaining at the initial fraction over the bulk of the layer beneath (e.g., Ref. [27]). Significant bulk viscosity [$\epsilon = O(1)$ or larger] mostly prevents the development of such a boundary-layer structure by assisting the diffusive spreading of the solid distribution (as shown by [15] and explored more fully including elasticity in Sec. V below).

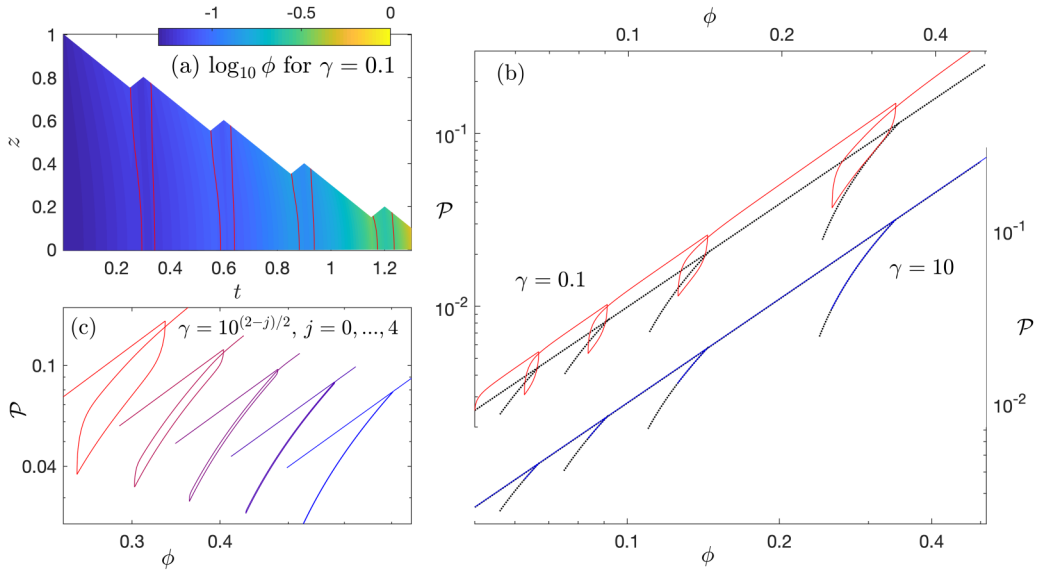

FIG. 6. Interrupted compression curves for differential compaction with $\epsilon = 10^{-2}$, $\gamma\lambda/\epsilon = 0.316$, $a = 3$, $n = m = 2$ and the values of γ indicated. Panel (a) shows the prescribed piston position $h(t)$, along with a density plot of $\log_{10}\phi$ for $\gamma = 0.1$; red contours indicate the yield surfaces where $\mathcal{P} = \Pi_\gamma(\phi)$. Two compression curves are shown in (b) (offset from one another); the black dotted lines show the corresponding quasistatic solution. Details of the loops arising during one unloading-reloading cycle are shown in (c), with γ ranging from 0.1 (red) to 10 (blue), offset successively (by factors of 1.2 and 1.1 in the horizontal and vertical, respectively) from the low-γ (red) loop for clarity.

In Fig. 6 we show an interrupted compression sequence for a material with both elasticity and bulk viscosity. In particular, we choose $\epsilon = 10^{-2}$ and $\gamma\lambda/\epsilon \equiv p_*/\mathcal{E}_* = 0.316$, which leads to modest viscous and elastic effects and compression behavior like that illustrated in Fig. 1(a). By fixing both ϵ and $\gamma\lambda/\epsilon$, but then varying γ, the theoretical problem corresponds to an experiment in which a given material is compressed at different rates. Solutions for varying dewatering rates (i.e., γ) are displayed in the figure using the interrupted compression sequence prompted by the motion of the piston indicated in Fig. 6(a). At the lowest dewatering rate ($\gamma = 10$), the layer remains spatially uniform and the compression curve matches up with $\Pi_\gamma(\phi)$ during the main compression sequence and the translated elastic stress curves $F(\phi) + \text{const}$ over the unloading-reloading cycles [see Fig. 6(b)].

For higher dewatering rates ($\gamma = 0.1$), the layer differentially compacts and the main compression curve shifts above $\Pi_\gamma(\phi)$ (cf. [15]). Moreover, the unloading-reloading cycles develop into loops. As the extent of these loops depends on the rate of dewatering [Fig. 6(c)], however, this feature cannot correspond to that observed in the relatively slow experiments of Sec. II C. Despite the differential compaction arising during the faster compressions, the layer largely plugs up once each unloading begins, and then yields once more after the reloadings have completed [see the yield surfaces plotted in Fig. 6(a)].

More differential compactions are shown in Figs. 7 and 8. In these two examples, fixed-rate compression occurs until the layer depth has halved, at which point the piston halts and the solid is left to relax under any remaining elastic stresses. By design, the constitutive model should capture both the phase of dynamic compression and the subsequent elastic recoil. In Fig. 7 the piston speed is constant until it stops abruptly at $t = \frac{1}{2}$ so that $h = \max(1 - t, \frac{1}{2})$; the second example shows a parabolic piston motion with compression trailing off more smoothly up to $t = 1$: $h = 1 - t + \frac{1}{2}t^2$ for $t \leqslant 1$, and $h = \frac{1}{2}$ for $t > 1$. Solutions for various values of λ are presented, with $\epsilon = \gamma = 10^{-2}$

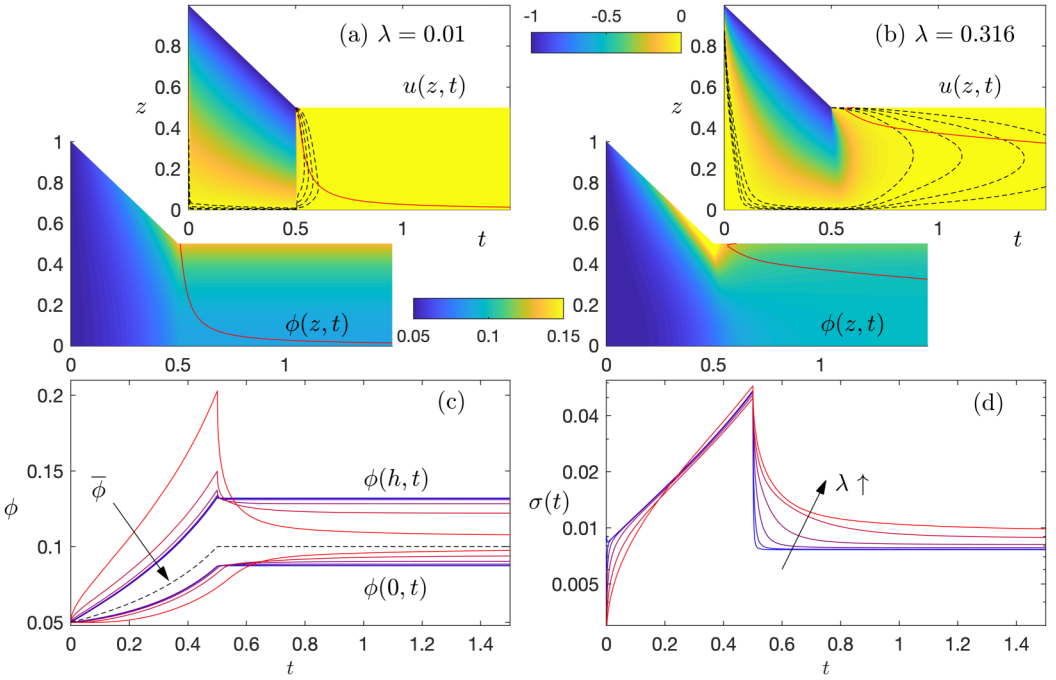

FIG. 7. Differential compaction for $\epsilon = \gamma = 10^{-2}$, $a = 3$, $n = m = 2$ using a constant piston speed up to $t = \frac{1}{2}$. Shown are density plots of velocity $u(z,t)$ and solid fraction $\phi(z,t)$ for (a) $\lambda = 0.01$ and (b) $\lambda = 0.316$. The red lines are the yield surfaces, and the black dashed lines show the contours $u = 2^j \times 10^{-3}$ for $j = 1, \ldots, 4$ to illustrate finer details not visible on this color scale. Below we plot time series of (c) the mean, top, and bottom solid fractions and (d) piston load, for solutions with $\lambda = 10^{(j-6)/2}$ for $j = 0, \ldots, 5$ (from blue to red).

and $n = m = 2$. Such choices correspond to compression tests with certain fixed rates, conducted on materials with different degrees of elasticity (i.e., λ). To ensure that the $F(\phi) \equiv \epsilon(\gamma\lambda)^{-1}\phi^2$ curve remains above $\Pi_Y(\phi) \equiv \phi^2$, we demand $\lambda < 1$.

Without elasticity ($\lambda \to 0$), some differential compaction arises, as illustrated by the solutions with $\lambda = 0.01$, for which elastic effects are minor. Once the piston halts, the layer quickly plugs up, with a yield surface descending from the piston. As elastic effects become more significant (larger λ), the degree of differential compaction during the compression phase increases; see panels (b) and (c) of the two figures. However, once the piston stops, the stored elastic stresses subsequently relax, decompressing the compacted boundary layer and eventually leaving a more uniform state than that reached without elasticity (panel c). The final elastic relaxation becomes protracted for the higher values of λ, unlike the viscoplastic layer which stops in its relaxed state instantaneously. The dashed contours of relatively small solid velocity included in panels (a) and (b) of the two figures highlight the residual motion that accompanies this relaxation (some of which is purely elastic once $\mathcal{P}$ falls below Π_Y).

With an abrupt halt to piston motion (Fig. 7), there is a sudden switch from compression under the piston to the elastic recovery. For an almost viscoplastic material, this switch is accompanied by a sharp fall in load as the viscous contribution to the solid stress is suddenly removed. Elasticity counters this drop in stress somewhat, although the load still falls sharply. When the piston slows more gradually (Fig. 8), the viscous stress on the piston declines much less precipitously, and any elastic recovery begins while the piston is still moving down. The sharp switch from compression to recovery is therefore avoided by bringing the piston to a smooth halt.

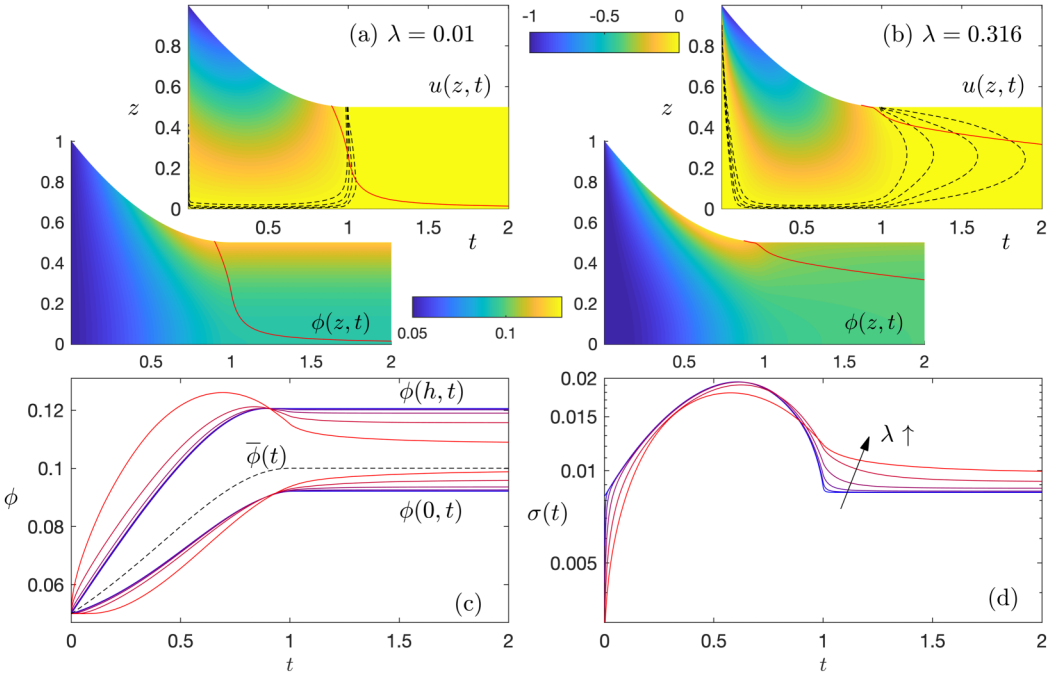

FIG. 8. A similar plot to Fig. 7, but with a parabolic piston motion for $t < 1$.

The enhancement of differential compaction by elasticity (increasing λ) is particularly noticeable with larger bulk viscosities (i.e., ϵ). In the viscoplastic model for $\epsilon = O(1)$, differential compaction is compensated by viscous spreading, with the solid remaining uniform even under relatively rapid compression ($\gamma \ll 1$) [15]. With sufficient elasticity, however, a compacted boundary layer can nevertheless appear underneath the piston as it descends, although most of this structure disappears under a protracted elastic recoil once the piston stops. These features are illustrated in Fig. 9(a), which plots the top and bottom solid fractions for solutions with $(\gamma, \epsilon) = (10^{-2}, 1)$ and different λ (i.e., the same γ but a larger ϵ than in Figs. 7 and 8). Without elasticity (the lower λ, blue curves), little differential compaction arises, with the solid fraction at the bottom closely tracking that at the top. By contrast, a sharp boundary layer develops as λ in increased. The boundary layer of the solution with $\lambda = 25$ is shown in more detail in Figs. 9(b) and 9(c), and compared to analytical results derived from the boundary-layer theory outlined in Sec. V. As illustrated by Fig. 9(d), the boundary layer forms for such parameters settings because the solid stress is dominated by elasticity, with $\mathcal{P}$ approaching the translated elastic stress function, $F = \epsilon(\phi^m - \phi_0^m)/(m\lambda\gamma) + \phi_0^n$. Consequently, the problem becomes governed by the nonlinear diffusion equation in Eq. (21), with a relatively small diffusivity D, setting the stage for the appearance of a boundary layer.

B. Fixed loading

Figure 10 shows a suite of solutions to the fixed-load compression problem. In these solutions, at $t = 0$ the top load is suddenly increased from $\mathcal{P}(h, t < 0) = \Pi_\gamma(\phi_0)$ up to $\mathcal{P}(h, t > 0) = R = 25\Pi_\gamma(\phi_0)$ [i.e., $\sigma(t > 0) = 1$], prompting differential compaction. Figures 10(a)–10(c) present solutions holding $p_*/\mathcal{E}_* \equiv \epsilon^{-1}\lambda = \frac{1}{4}$ fixed and varying ϵ; solutions with $\epsilon = 0.01$ and varying λ are presented in Fig. 10(d). Because γ is scaled to 1 in this problem (see the introduction to Sec. IV) and $\epsilon \propto h_0^{-2}$, the former [Figs. 10(a)–10(c)] corresponds to a fixed-load problem with, for example, a given material but varying initial depth. The latter [Fig. 10(d)] corresponds to a particular loading problem for materials with differing elastic moduli.

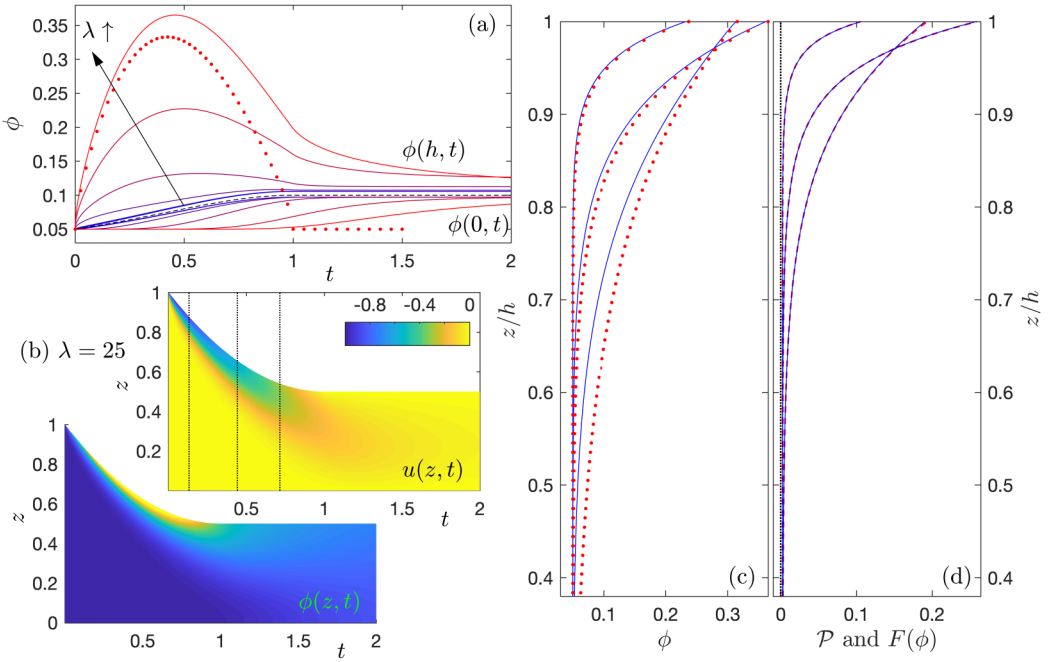

FIG. 9. Parabolic compression solutions with $\epsilon = 1$, $\gamma = 0.01$ and $a = n = m = 2$. Time series of the bottom and top solid fractions, $\phi(0,t)$ and $\phi(h,t)$, are plotted in (a) for $\lambda = 0.01$, 0.1, 1, 4, 12.5, and 25 (blue to red). Also shown are the mean solid fraction $\overline{\phi}(t)$ (dashed) and the prediction in Eq. (36) (red dots). For the solution with $\lambda = 25$, we present (b) density plots of $u(z,t)$ and $\phi(z,t)$, and the profiles of (c) $\phi(z,t)$ and (d) $\mathcal{P}(z,t)$ at the times indicated by the dotted lines in (b). The (red) dots in (c) show the prediction from Eq. (33), based on the value of ϕ_T from the numerical solution, and the (red) dashed lines in (d) show the translated elastic stress function $F = \epsilon(\phi^m - \phi_0^m)/(m\lambda\gamma) + \phi_0^n$.

The sudden loading causes the piston to descend abruptly, and a compacted boundary layer develops underneath. This is illustrated in Figs. 10(a), 10(c), and 10(d), which plot time series of $h(t)$ and the top and bottom solid fractions for the two series of solutions, and Fig. 10(b), which shows the structure of the boundary layers for the problem with fixed λ/ϵ. In Fig. 10(b), the boundary-layer profiles of $\phi(z,t)$ are again compared with the predictions of the theory in Sec. V.

The time series of solid fraction [Figs. 10(c) and 10(d)] display distinctive features reflecting the degree to which elasticity impacts the loading problem: except at the lowest values for λ, the boundary layer becomes dominated initially by the elastic stress, with the top solid fraction adjusting to the value ϕ_E for which the load is balanced by the elastic stress function:

$$F(\phi_E) - F(\phi_0) + \Pi_Y(\phi_0) = R, \tag{25}$$

or, given the specific parameters used here,

$$\epsilon\lambda^{-1}\left(\phi_E^2 - \phi_0^2\right) = 24. \tag{26}$$

For the smallest values of λ, however, the elastic stress does not limit the compaction in the boundary layer, which instead becomes controlled by the compressive yield stress. The top solid fraction then approaches the value set by $\Pi_Y(\phi_\infty) = R$, or $\phi_\infty = 5\phi_0$. These two features are illustrated in Figs. 10(c) and 10(d), where the redder curves of $\phi(h,t)$, with higher λ or ϵ, first level off at ϕ_E, whereas the blue curves, with lower λ and ϵ, progress with little interruption up to ϕ_∞.

Somewhat later, the piston slows down, prompting elastic effects to decrease relative to plastic ones (cf. Sec. V). If, at this stage, the solid still remains compacted against the piston [so that $\phi(0,t)$

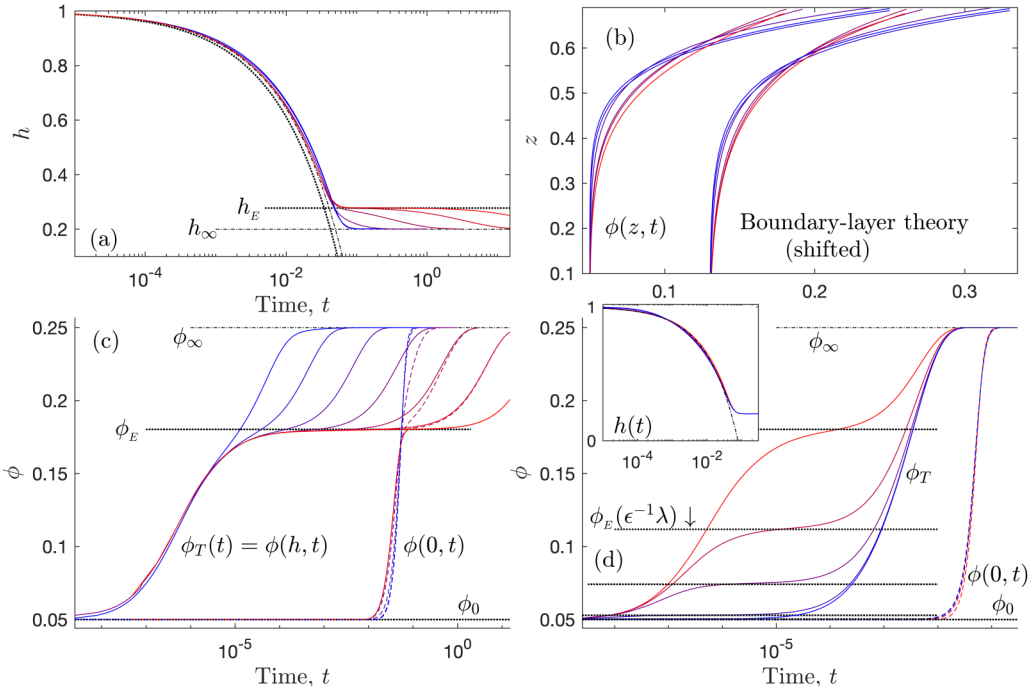

FIG. 10. Fixed-load compression ($\gamma = 1$) with $a = n = m = 2$ and $R = 25\Pi_{\gamma}(\phi_0)$. In (a)–(c) $\epsilon^{-1}\lambda = \frac{1}{4}$ and $\epsilon = 10^j$ for $j = -4, -3, \ldots, 2$ (blue to red). Shown are (a) $h(t)$, (b) spatial profiles of $\phi(z,t)$ when $h \approx 0.69$, and (c) $\phi_T(t) = \phi(h,t)$ and $\phi(0,t)$. The horizontal lines in (a) and (c) show (ϕ_E, h_E) (dotted) and (h_∞, ϕ_∞) (dot-dashed); the corresponding curves show Eq. (37) for the elastic and plastic limits. Also shown in (b) (shifted to the right for clarity) are predictions from Eq. (33), based on the values of ϕ_T from the numerical solutions. Panel (d) shows a similar plot to (c), but for solutions with $\epsilon = 0.01$ and $4\epsilon^{-1}\lambda = 1, \frac{1}{3}, 10^{-1}, 10^{-2}$, and 10^{-3} (from red to blue). The inset shows $h(t)$.

remains at ϕ_0], the boundary layer accordingly adjusts its structure from that controlled by elasticity to that imposed by the yield stress [see the purple solutions for $\phi(h,t)$ with intermediate values for ϵ and λ in Fig. 10(c), and the redder curves for larger λ in Fig. 10(d)]. Somewhat later, the boundary layer reaches the bottom, $\phi(0,t)$ catches up to $\phi(h,t)$, and a spatially uniform final state is approached with $\phi = \phi_\infty$ and $h = h_\infty \equiv \phi_0/\phi_\infty = \frac{1}{5}$, for the specific case considered here.

For the highest values of λ and ϵ [the red curves in Figs. 10(a)–10(c)], the boundary layer reaches the bottom before compressive yield stresses take hold. A different spatially uniform state then emerges with $\phi \approx \phi_E$ and $h = h_E = \phi_0/\phi_E$. Eventually the stress again relaxes, however, and the layer approaches the same final state as for smaller ϵ. That equilibrium, with $\phi = \phi_\infty$, is demanded regardless of the parameters settings (provided $F > \Pi_{\gamma}$) because the load always raises the stress above $\Pi_{\gamma}(\phi)$ and the solid is unable to fall back below that yield stress during compaction. The final approach to steady state is therefore always controlled by the plastic stress, and the corresponding nonlinear diffusion equation in Eq. (21). This is unlike the fixed-rate problem, for which the layer begins to unload when the piston halts, allowing the stress to fall below Π_{γ}, which freezes into place the differentially compacted solid distribution.

V. BOUNDARY-LAYER THEORY

A useful exercise in understanding the dynamics captured by the model and interpreting the impact of parameter variations is to consider the limit in which the descent of the piston generates

a narrow compacted layer just underneath. Such boundary layers were considered in [15] for the plastic problem. For the current model, we first transform into a frame moving with the piston by setting $\zeta = h - z$; in this frame, spatial derivatives must be large and the mass conservation equation becomes

$$[(u - \dot{h})\phi]_\zeta \approx \phi_t. \tag{27}$$

In principle, we should neglect the right-hand side of this equation in comparison to the left-hand side, and then integrate to find that $(u - \dot{h})\phi$ is some function of time alone. However, $u = \dot{h}$ at $\zeta = 0$, but $(\phi, u) \to (\phi_0, 0)$ below the boundary layer, which offer conflicting choices for the constant. In particular, because $\zeta = 0$ is contained within the boundary layer the first condition is potentially the more natural, but this implies $u \sim \dot{h}$ throughout the finely structured region and is inconsistent with the stationary layer underneath. The issue is connected to how, after a finite time, an $O(\phi_0)$ amount of solid is compressed into the relatively thin boundary layer, and so the solid fraction there is necessarily much greater than ϕ_0 by a factor of order δ^{-1}, where δ measures the thickness of the boundary layer.

To resolve this conflict, we avoid neglecting the right-hand side of Eq. (27), and instead evaluate it perturbatively. More specifically, the quasistatic boundary-layer structure is expected to take the form,

$$S(\phi) = S(\phi_T) + \zeta, \quad \phi_T(t) = \phi(0, t), \tag{28}$$

for some function $S(\phi)$. For the perfectly plastic or elastic problems, satisfying Eq. (21), we have explicitly $S(\phi) \equiv \int \phi^{-1} D(\phi) d\phi$. This functional form implies that

$$\phi_t = \dot{\phi}_T S'(\phi_T)\phi_\zeta \quad \text{and} \quad \int_0^\zeta \phi_t d\zeta = -\dot{\phi}_T S'(\phi_T)(\phi_T - \phi). \tag{29}$$

But mass conservation demands [since $\phi \to \phi_0$ for $\zeta \to h(t)$]

$$0 = \frac{d}{dt}\int_0^h \phi(\zeta, t)\, d\zeta = \int_0^h \phi_t d\zeta + \dot{h}\phi_0. \tag{30}$$

Hence

$$u = \dot{h} + \phi^{-1}\int_0^\zeta \phi_t\, d\zeta \approx \frac{\dot{h}\phi_T(\phi - \phi_0)}{\phi(\phi_T - \phi_0)}, \tag{31}$$

which now satisfies both of the originally conflicting conditions and reduces to $u \sim \dot{h}$ if $(\phi, \phi_T) \gg \phi_0$.

Next, since $\mathcal{P} = \Pi_\gamma(\phi)$ or $\mathcal{P} = F(\phi) - F(\phi_0) + \Pi_\gamma(\phi_0)$ in the plastic or elastic boundary layers, we set

$$\frac{D\mathcal{P}}{Dt} \sim \frac{\mathcal{P}_\zeta}{\phi_\zeta}\frac{D\phi}{Dt} \sim \frac{\dot{h}^2\phi_0\phi_T^2(\phi - \phi_0)}{\gamma K\phi^2(\phi_T - \phi_0)^2}. \tag{32}$$

Assuming $\mathcal{P} > \Pi_\gamma$, we may now differentiate the constitutive law and rearrange the resulting expression into

$$K\phi_0\left\{\frac{\Lambda}{\phi^2}\left[\epsilon\phi_\zeta - \frac{\lambda\dot{h}\phi_T(\phi - \phi_0)}{EK(\phi_T - \phi_0)}\right]\right\}_\zeta \sim 1 - \frac{\phi_0}{\phi} - \frac{(\phi_T - \phi_0)}{\dot{h}\phi_T}\gamma K\Pi_\gamma{}'\phi_\zeta. \tag{33}$$

Omitting the left-hand side furnishes a boundary-layer theory for the perfectly plastic problem; neglecting the right-hand side gives the elastic version. In all cases, we must solve Eq. (33) subject to $\phi(0, t) = \phi_T$ and $\phi(h, t) = \phi_0$, and then feed the result into the mass conservation constraint $\int_0^h \phi\, d\zeta = \phi_0$. For fixed piston position, $h(t)$, this procedure determines $\phi_T(t)$. For fixed load, on the other hand, the top boundary condition demands $\mathcal{P} = R\Pi_\gamma(\phi_0)$ with either $\mathcal{P} \sim \Pi_\gamma(\phi_T)$ or

$\mathcal{P} \sim F(\phi_T) - F(\phi_0) + \Pi_\gamma(\phi_0)$, both of which fix the solid fraction at the top. The mass conservation constraint then corresponds to a differential equation for the piston position because $\dot{h}$ appears explicitly in Eq. (33).

Away from the plastic and elastic limits, Eq. (33) offers a means of deciphering the controlling factors for the solid distribution and determining the boundary-layer thickness δ. For the viscoplastic model, the action of the bulk viscosity in delocalizing the boundary layer is evidenced by the first term. The second, elastic contribution is similar to that from the compressive yield stress (final term on the right-hand side), although its opposite sign is indicative that larger λ solutions should show a sharpening of the boundary layer relative to the viscoplastic theory, as observed numerically. Moreover, the different dependence of these terms on the instantaneous compression rate $\dot{h}$ emphasizes how elasticity is promoted at faster rates and plasticity for lower rates.

The prediction of Eq. (33) for the solid distribution appears along with the numerical computations in Figs. 9 and 10, adopting the instantaneous value of ϕ_T computed numerically. The solution in Fig. 9 is, in fact, controlled largely by elastic stresses, as is illustrated by Fig. 9(d), which demonstrates that $\mathcal{P}(z,t)$ remains close to the (translated) elastic stress function $F = \epsilon(\phi^m - \phi_0^m)/(m\lambda\gamma) + \phi_0^n$ during the compression. In this situation, the main balance in Eq. (33) is between the first two terms, leading to a characteristic boundary layer scale of $\delta \sim \epsilon EK/(\lambda|\dot{h}|)$. For the solution in Fig. 9, this scale is $\delta \sim [25(1-t)]^{-1}$ which roughly matches the half-width of the boundary-layer profiles displayed in Fig. 9(c).

For the perfectly plastic limit [$\epsilon = \lambda = 0$, omitting the left-hand side of Eq. (33)], we obtain

$$\dot{h}\phi_T(\phi - \phi_0) = (\phi_T - \phi_0)D\phi_\zeta, \tag{34}$$

with $D = \gamma\phi K\Pi_{\gamma'}$ (indicating that the characteristic boundary layer thickness is now $\delta \sim \gamma K\Pi_{\gamma'}/|\dot{h}|$). An integral of Eq. (34) over the layer gives

$$-\dot{h}\phi_T\phi_0(1-h) = (\phi_T - \phi_0)\int_{\phi_0}^{\phi_T} D(\phi)\,d\phi. \tag{35}$$

For the perfectly elastic limit [neglecting the right-hand side of Eq. (33)], we recover exactly the same result, but with $D \equiv \epsilon\lambda^{-1}EK$, as in Eq. (22). Note that, if $\phi K\Pi_{\gamma'} = \text{const}$ or $EK = 1$ (i.e., $a = n$ or $a = m$), then the diffusivity D is constant in either limit (and equal n or ϵ/λ), and so

$$\phi_T = \phi_0\left[1 + \frac{1}{2}\mathcal{T} + \sqrt{\mathcal{T}\left(1 + \frac{1}{4}\mathcal{T}\right)}\right], \tag{36}$$

for fixed rate with $\mathcal{T} = -D^{-1}\dot{h}(1-h)$, or

$$h = 1 - (\phi_T - \phi_0)\sqrt{\frac{2Dt}{\phi_T\phi_0}}, \tag{37}$$

for fixed load.

A key limitation in these results is the condition $\phi(h,t) = \phi_0$, which fails when the boundary layer reaches the bottom. Equation (33) also cannot capture any final elastic recoil: in this setting $\dot{h} = 0$ and we must omit the right-hand side in view of the yield condition, leaving only $\phi_{\zeta\zeta} = 0$ (and implying that the time derivatives have not been dealt with adequately). Both limitations are visible in Fig. 9(b), which includes the prediction in Eq. (36): as time advances, the boundary layer thickens and the adjustments in solid fraction reach the base, both of which cause the prediction to diverge from the numerical solution with time. Moreover, for $t > 1$, the piston stops with the boundary-layer theory predicting that ϕ_T returns to ϕ_0 (the theory effectively assumes that the medium has infinite depth, and so the predicted solid fraction at the top is allowed to fall below $\overline{\phi} = h^{-1}$). The latter issue also plagues the predictions for the fixed load problems shown in Fig. 10, which compares the numerically computed $h(t)$ with the result from Eq. (37), taking $D = \epsilon\lambda^{-1}$ [Fig. 10(a)] or $D = 2$ [Fig. 10(a) and the inset to 10(d)].

VI. RAPID DEWATERING OF CELLULOSE SUSPENSIONS

A. Experimental description and materials

The experimental apparatus is a filtration device that uses a MTS 858 tabletop material tester operated remotely by a control unit. The MTS pushes a permeable piston into a cylinder of radius 6.7 cm holding the suspension. The cylinder is positioned on top of a load cell that measures $\hat{\sigma}(\hat{t})$. The piston fits closely into the cylinder, and a friction force between the piston seals and the walls of 6500 Pa is subtracted from the load measurements during fixed-rate compressions. The unit is capable of providing compression loads of 1.0–1.2 MPa.

The $\hat{h}(\hat{t})$ compression profile chosen for the dewatering experiments is parabolic, which has the benefit of gradually stopping the piston while starting with a relatively high speed. With a LABVIEW interface, we specify initial suspension height h_0, end height $h_0 h_{\rm end}$, and the initial compression rate $U = -\dot{h}_0$, so that the dimensionless height of the piston $h = \hat{h}/h_0$ is given by

$$h = \begin{cases} 1 - t + t^2/[4(1 - h_{\rm end})], & t \leqslant 2(1 - h_{\rm end}), \\ h_{\rm end}, & 2(1 - h_{\rm end}) < t, \end{cases} \tag{38}$$

written in terms of the same dimensionless time $t = (U/h_0)\hat{t}$ as in Eq. (13). This imposed height profile thus has the same form as that considered theoretically in Fig. 8. For the dewatering tests, we set $h_0 = 41.4$ cm and $h_0 h_{\rm end} = 5.6$ cm, leaving the initial compression rate as the main parameter. The interface was also used to calibrate the network's elastic response, by performing slow compressions interrupted by unloading-reloading cycles (see Sec. II C). The cycles were performed by unloading the suspension to 66% of the load at which the piston reversal started, fixing the piston speed at ± 1 μm/s.

The cellulose suspension is composed of a northern bleached softwood kraft (NBSK) wood pulp, consisting of a mixture of Scots Pine and Norway Spruce [35]. The suspensions are made from dried pulp sheets, and prepared to an initial concentration of $\phi_0 \approx 0.025$ for the dewatering tests. Calibrations of the compressive yield stress and permeability were undertaken in [19], resulting in the fits

$$P_Y(\phi) = 6.20\times 10^5 \phi^{1.87}(1 - \phi)^{-3.83} \text{ Pa} \tag{39}$$

and

$$k(\phi) = 2.67\times 10^{-13}\phi^{-1} \ln \phi^{-1} e^{-20.38\phi} \text{ m}^2, \tag{40}$$

as shown in Fig. 11. The bulk viscosity scaling was also fitted to be $\eta_* = 2.89\times 10^7$ Pa [19], based on tests conducted at lower compression rates than those we report below. The unloading-reloading cycles conducted here further provided the bulk modulus $\mathcal{E}(\phi)$, also included in Fig. 11(a). The closed squares are measured by the MTS; the open circles were determined by an additional low-load experimental apparatus using the same protocol (slow compaction and partial unloading) [18]. The fit to the combined data is

$$\mathcal{E}(\phi) = 1.08\times 10^8 \phi^{2.71}(1 - \phi)^{-0.688} \text{ Pa}. \tag{41}$$

Although the fitted forms for P_Y Eqs. (39) and $\mathcal{E}$ (41) look quite different, the actual functional forms are remarkably similar, but for a constant factor of about 20, as can be seen in Fig. 11. This similarity suggests a common physical origin for the plastic and elastic components of the stress in this suspension, such as might arise if the friction incurred by plastic re-arrangements was controlled by the elastic normal forces arising from the bending or collapse of fiber walls (cf. [19]).

Below we present the experimental results for dynamic dewatering. When we compare these observations with theory, and employ dimensionless variables, we use a nominal solid fraction $\phi_* = 0.1$ in order to select the characteristic scales $p_* = P_y(\phi_*)$, $\mathcal{E}_* = \mathcal{E}(\phi_*)$, and $k_* = k(\phi_*)$. In terms of the dimensionless groups defined in Sec. III that then emerge, we note that the experiments are

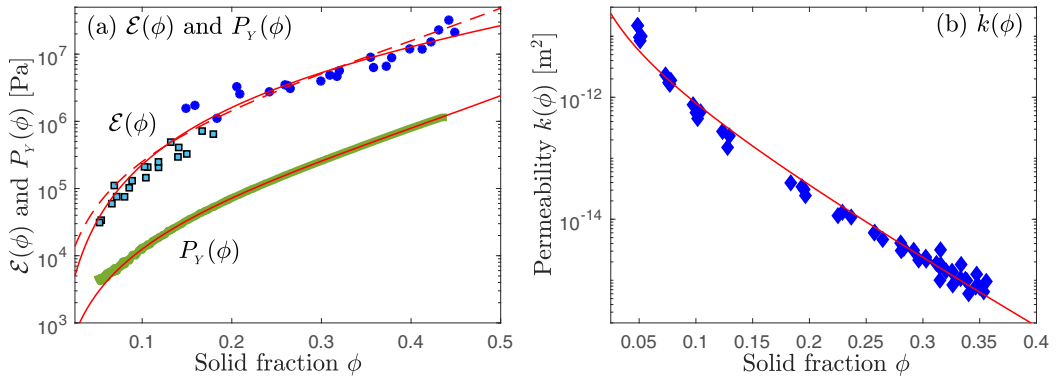

FIG. 11. Fitted constitutive functions for the pulp suspension, showing (a) $P_Y(\phi)$ and $\mathcal{E}(\phi)$ and (b) permeability. The symbols show the actual experimental measurements; the solid red lines are the fits. The dashed red line in (a) shows the fit for P_Y multiplied by a factor of 20. The lighter blue symbols denote results obtained from the low-load tests reported by [18].

conducted with parameters

$$\epsilon = 13.5, \quad 4\times10^{-3} \leqslant \gamma = 0.049(U/U_*)^{-1} \leqslant 0.049, \quad 15.4 \leqslant \lambda = 15.4(U/U_*) \leqslant 185,$$

where $U_* = 5$ mm/s. Thus, without elasticity, we expect dewatering to be relatively rapid ($\gamma \ll 1$) but the bulk viscosity to significantly smooth the solid distribution (ϵ is large). However, elasticity is also likely to be important ($\lambda \gg 1$).

B. Dynamic dewatering

Experimental compression curves were collected for a variety of initial piston velocities U. Sample results are presented in Fig. 12. This figure plots recorded load against time, both dimensionless. As the initial compression rate U increases, the load rises more steeply, then falls as the piston slows down. Visual observations of the suspension in the cup indicate that the steepening rise of the load

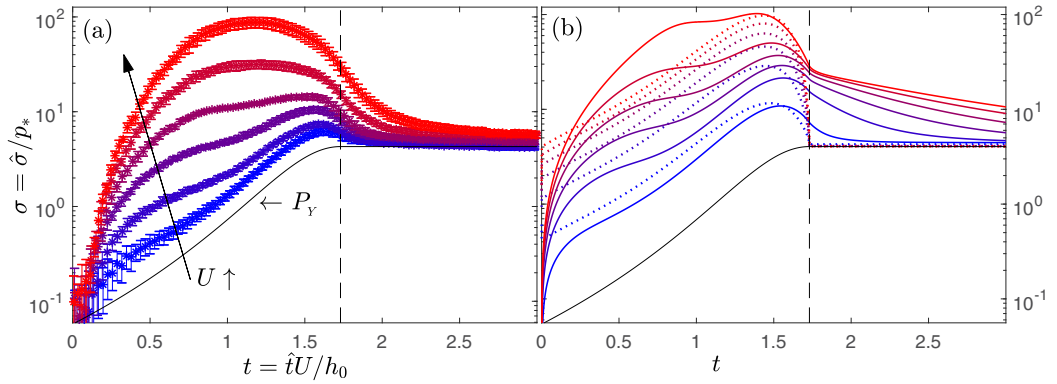

FIG. 12. Compressions for cellulose fibers performed at varying initial velocities ($U = 5, 15, \ldots,$ 55 mm/s) with the same initial and final heights. Panel (a) shows experimental results. Each test is conducted four times; the points show the average and the error bars band a standard deviation. Panel (b) shows the corresponding results for the theoretical model with (solid) and without (dotted) elasticity. The vertical dashed line indicates when the piston stops, and the black line shows the load assuming that compression arises quasistatically along the P_Y curve.

is associated with enhanced differential compaction, with pulp packing into a boundary layer under the permeable piston, as observed in other studies [36–38]. Eventually, the boundary layer stops packing as the piston decelerates and the load drops, much as in the theoretical solutions presented in Sec. III.

Figure 12 also reports matched theoretical results, both with and without elasticity. For the lowest compression rates there is only a minor difference between the two versions of the model, with the elastic theory performing slightly better in reproducing the experiment. This reflects the conclusions of [15,19], which found that the inclusion of a bulk viscosity alone was effective in allowing the model to reproduce experimental dewatering behaviors at these compression rates. Indeed, if neither elasticity nor a viscous solid stress is included ($\lambda = \epsilon = 0$) and $\mathcal{P} = \Pi_y(\phi)$, the model predicts that the solid immediately packs to unphysically high concentrations underneath the piston, generating excessive loads, at the compression speeds used in Fig. 12 (cf. [15,19]).

For faster compressions, the elastic version of the model noticeably outperforms the viscoplastic model in reproducing both the shape and magnitude of the load curves in Fig. 12. In particular, the viscoplastic model predicts that the load rises abruptly at the earliest times, but then climbs more slowly; the smoother initial rise in $\hat{\sigma}(t)$ for the elastic solutions, followed by an elevated load for $0.1 < t < 1.1$, more closely matches the experimental results.

The final relaxation of the stress is also poorly reproduced by the model without elasticity: with $\lambda \to 0$, the model load abruptly stabilizes at its final value when the piston stops. The experiments display a more gradual trend, however, more like the elastic relaxation of the model with finite λ. That said, the theoretical results with the calibrated values for the material functions display a more pronounced final relaxation than the experiments, and the agreement between the two sets of load curves is only qualitative.

C. Particle tracking

Although the elastic-viscoplastic model performs better than the viscoplastic version of the model in reproducing load curves, the improvement is not dramatic, leading one to wonder whether the addition of elasticity is truly key. However, for the relatively significant values of the bulk viscosity found for the pulp suspension [for which $\epsilon = O(1)$], the purely viscoplastic model is expected to predict that little differential compaction should arise during compression (see Sec. IV A). But provided elastic effects are sufficiently strong, a boundary layer can build underneath the piston as it descends. This is, indeed, what is observed experimentally, with the suspension deforming far from uniformly in space.

To pursue this detail further, we performed particle tracking on the solid during the compression tests. The tracking tests were performed using a smaller range of compression and initial solid fraction, with $(h_0, h_0 h_{\text{end}}) \approx (5.4, 2)$ cm and $\phi_0 \approx 0.02$, to ease the identification of the tracer particles. Sample results are shown in Fig. 13, which plots the observed solid velocities as densities over the (t, z) plane. Also displayed are the predictions of the elastoviscoplastic and purely viscoplastic models. At relatively low compression rate (left-hand column), the two versions of the model are largely in agreement and predict similar solid velocities as those observed (which again coincides with the findings of [15,19]). The only noteworthy discrepancy is that the viscoplastic model predicts a sudden onset of motion throughout the solid (a feature connected with the abrupt initial rise of the load seen in Fig. 12 for the dotted curves). Instead, with elasticity, a signal descends through the layer, activating motion. The particle-tracking data support the latter behavior, although the measurements are not especially definitive.

As the dewatering speed U is increased (progressing from left to right in Fig. 13), this discrepancy becomes more obvious, with the solid velocity becoming strongly confined to a layer underneath the piston for both the particle tracking measurements and the elastic model. This feature reflects the buildup of a compacted boundary layer, as found in our general theoretical exploration of the model when the bulk solid viscosity is either small ($\epsilon \ll 1$) or if elasticity is important [$\lambda = O(1)$ or larger]; see Sec. IV. For the parameter settings expected for the experiments, the bulk viscosity

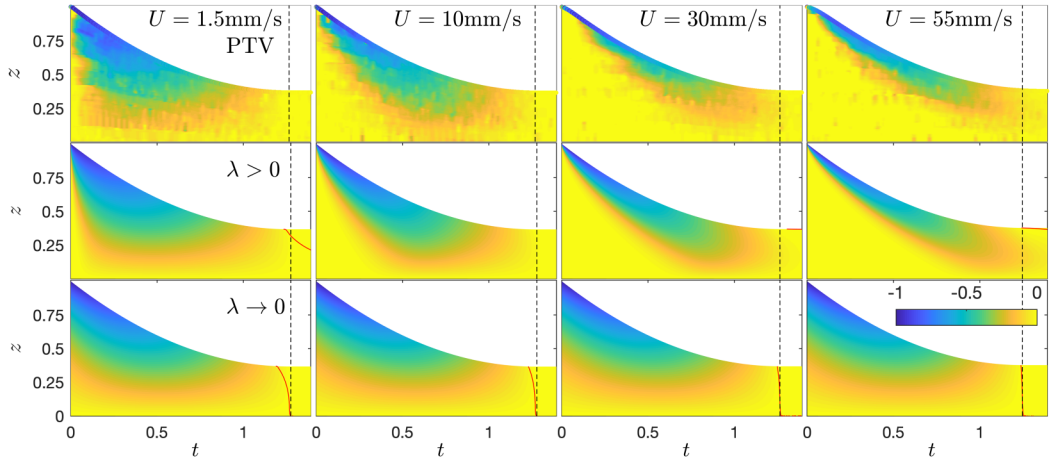

FIG. 13. Solid velocities, $u(z,t) = \hat{u}/U$, as densities on the (t,z) plane for $U = 1.5$, 10, 30, and 55 mm/s (from left to right). For each column, particle tracking measurements are shown on the top, the predictions of the elastoviscoplastic theory in the middle, and those of the viscoplastic model on the bottom. The vertical dashed lines show where the piston stopped, and the red contours in the theoretical plots show the yield surfaces. The PTV data include the velocities computed for the piston.

is relatively large [$\epsilon = O(10)$]. As a result, the solid distribution in the purely viscoplastic model is excessively smoothed by the bulk solid viscosity, and no boundary layer emerges if $\lambda \to 0$. Instead, the solid velocity extends down to the base of the layer immediately from the beginning of the piston's descent, and the space-time plot of u looks similar for all the different compression speeds (see the bottom row of panels in Fig. 13). By contrast, the particle tracking measurements reveal definitively that the differential solid motion is dependent on piston speed and becomes confined to a boundary layer for higher compression rates, in agreement with the elastoviscoplastic model (top and middle rows in Fig. 13).

VII. DISCUSSION

In this paper we have explored a model for the compaction of a two-phase medium in which the solid is allowed to deform elastoviscoplastically. The model borrows a constitutive law for the solid stress from theory of single-phase complex fluids and couples that with traditional formulations for two-phase media. Previous models for the compression of soils or colloidal suspensions often prescribe the solid stress as a material function of the local solid concentration, which in the two-phase formulation leads to similar mathematical formulations, with the elastic or plastic origin of the stress becoming secondary. By contrast, our current model distinguishes between purely elastic or plastic deformation and accommodates a solid viscous response that has proved previously to be effective in model comparisons with experiments for certain media. The model also permits one to examine the dynamics of a medium that is first compressed and then unloaded, which naturally differentiates elastic recovery from the hysteresis originating from plastic deformation.

To interrogate the theoretical model, we considered one-dimensional compression and unloading with either fixed rate or fixed load. In such problems, boundary layers of compacted solid can appear against the permeable walls when compression is relatively fast. We provided further analysis of such situations, constructing some asymptotic solutions or reductions of the model equations that can be used to further dissect the problem.

We then confronted the model with the reality of an experiment conducted using a suspension of cellulose fibers. Earlier experimental investigations with such materials had shown the need for a solid viscous-like stress to explain the compaction dynamics. The tests that we conducted here used

faster rates of compression and also considered unloading, both aimed at promoting or identifying elastic effects. The experiments were in qualitative agreement with the theoretical model, once certain material functions (the dependence of the permeability, compressive stress, elastic bulk modulus, and viscosity) were calibrated. In particular, using particle tracking of tracers in the solid, we were able to demonstrate that the elastoviscoplastic model was capable of reproducing the differential spatial compaction, as well as the net load exerted on the piston performing the compression.

Despite this qualitative agreement, there are quantitative discrepancies between the model and experiment. In view of the relative crudeness of the model, which was posed in the interest of simplicity, this is perhaps not so surprising. One obvious possible origin of the lack of quantitative agreement is the bulk viscosity function that we adopted, $\hat{\Lambda} = \eta_* \phi^2$. Unlike our other material functions, the dependence of this quantity on solid fraction has not been directly measured. Instead, the functional form was assumed, and the fitting parameter η_* determined by comparing model solutions for dynamic dewatering with experiments. Part of the discrepancy between theory and experiment could therefore originate from a failure to calibrate correctly the ϕ dependence of the rate-dependent part of the solid stress. A better approach would be to perform additional time-dependent tests to calibrate this function properly, as is typically done in rheometry of complex fluids.

A more serious issue is the failure to explain the loops that appear in quasistatic compression curves that are interrupted by cycles of unloading and reloading. Measurements for cellulose fiber suspensions (Sec. II C; [18]) demonstrate that the cycle creates a stress-strain loop that appears to be independent of rate, much as for other materials (cf. [8,14,39–42]). Only with differential spatial compaction do loops appear for the model, and even then, they are rate-dependent. The same issue has been encountered in soil mechanics, where attempts have been made to account for the loop by introducing limitations on elastic strains at the granular level [43–46]. However, these modifications are made to constitutive descriptions that are rather more complicated than that considered here, and it is not clear how such ideas could be incorporated into the present model.

ACKNOWLEDGMENT

Financial assistance from both Valmet Ltd and the Natural Sciences and Engineering Research Council of Canada Grant No. CRDPJ 479552-15, is gratefully acknowledged. We thank Dr. Tomas Vikström and Jean-Pierre Bousquet for constructive comments.

[1] O. Coussy, *Poromechanics* (Wiley, New York, 2004).
[2] A. C. Fowler, *Mathematical Geoscience*, Interdisciplinary Applied Mathematics (Springer-Verlag, London, 2011), Vol. 36.
[3] A. H.-D. Cheng, *Poroelasticity, Theory and Applications of Transport in Porous Media*, Poroelasticity, Theory and Applications of Transport in Porous Media (Springer, Cham, Switzerland, 2016), Vol. 27.
[4] R. Buscall and L. R. White, The consolidation of concentrated suspensions. Part 1. The theory of sedimentation, J. Chem. Soc. Faraday Trans. **83**, 873 (1987).
[5] K. A. Landman and L. R. White, Solid/liquid separation of flocculated suspensions, Adv. Colloid Interface Sci. **51**, 175 (1994).
[6] F. Concha and R. Bürger, A century of research in sedimentation and thickening, KONA Powder Particle J. **20**, 38 (2002).
[7] R. G. de Kretser, D. V. Boger, and P. J. Scales, Compressive rheology: An overview, Rheol. Rev. **1**, 125 (2003).
[8] J. I. Dunlop, On the compression characteristics of fibre masses, J. Text. Inst. **74**, 92 (1983).
[9] T. Murase, M. Iwata, M. Wakita, T. Adachi, N. Hayashi, and M. Shirato, Expansion of consolidated material after release of load, J. Chem. Eng. Jpn. **22**, 195 (1989).

[10] V. Lobosco and V. Kaul, An elastic/viscoplastic model of the fibre network stress in wet pressing: Part 1, Nord. Pulp Pap. Res. J. **16**, 12 (2001).
[11] V. Lobosco and V. Kaul, The stress-strain relationship of the fibre network in wet pressing, Nord. Pulp Pap. Res. J. **20**, 24 (2005).
[12] P. A. Kelly, R. Umer, and S. Bickerton, Viscoelastic response of dry and wet fibrous materials during infusion processes, Composites A: Appl. Sci. Manuf. **37**, 868 (2006).
[13] C. W. MacMinn, E. R. Dufresne, and J. S. Wettlaufer, Fluid-Driven Deformation of a Soft Granular Material, Phys. Rev. X **5**, 011020 (2015).
[14] D. R. Hewitt, J. S. Nijjer, M. G. Worster, and J. A. Neufeld, Flow-induced compaction of a deformable porous medium, Phys. Rev. E **93**, 023116 (2016).
[15] D. R. Hewitt, D. T. Paterson, N. J. Balmforth, and D. M. Martinez, Dewatering of fibre suspensions by pressure filtration, Phys. Fluids **28**, 063304 (2016).
[16] T. S. Eaves, D. T. Paterson, D. R. Hewitt, N. J. Balmforth, and D. M. Martinez, Dewatering saturated, networked suspensions with a screw press, J. Eng. Math. **120**, 1 (2019).
[17] D. T. Paterson, T. S. Eaves, D. R. Hewitt, N. J. Balmforth, and D. M. Martinez, Flow-driven compaction of a fibrous porous medium, Phys. Rev. Fluids **4**, 074306 (2019).
[18] D. T. Paterson, Understanding the dynamics of dewatering pulp fibre suspensions, Ph.D. thesis, University of British Columbia, 2020.
[19] D. T. Paterson, T. S. Eaves, D. R. Hewitt, N. J. Balmforth, and D. M. Martinez, On two-phase modeling of dewatering pulp suspensions, AIChE J. **67**, e17277 (2021).
[20] F. El-Hosseiny, Compression behavior of press felts and wet webs, Nord. Pulp Pap. **5**, 28 (1990).
[21] A. Swerin, Rheological properties of cellulosic fibre suspensions flocculated by cationic polyacrylamides, Colloids Surf. A **133**, 279 (1998).
[22] H. Vomhoff and A. Schmidt, The steady-state compressibility of saturated fibre webs at low pressures, Nord. Pulp Pap. Res. J., 12 (1997).
[23] M. J. Patel, S. Blackburn, and D. I. Wilson, Modelling of pastes as viscous soils—Lubricated squeeze flow, Powder Technol. **323**, 250 (2018).
[24] P. Saramito, A new constitutive equation for elastoviscoplastic fluid flows, J. Non-Newtonian Fluid Mech. **145**, 1 (2007).
[25] M. H. Holmes, A nonlinear diffusion equation arising in the study of soft tissue, Q. Appl. Math. **41**, 209 (1983).
[26] S. I. Barry and G. K. Aldis, Unsteady flow induced deformation of porous materials, Int. J. Non-Linear Mech. **26**, 687 (1991).
[27] K. A. Landman, C. Sirakoff, and L. R. White, Dewatering of flocculated suspensions by pressure filtration, Phys. Fluids A: Fluid Dyn. **3**, 1495 (1991).
[28] D. M. Audet and A. C. Fowler, A mathematical model for compaction in sedimentary basins, Geophys. J. Int. **110**, 577 (1992).
[29] R. Bürger, F. Concha, and K. H. Karlsen, Phenomenological model of filtration processes: 1. Cake formation and expression, Chem. Eng. Sci. **56**, 4537 (2001).
[30] M. Shirato, T. Murase, A. Tokunaga, and O. Yamada, Calculations of consolidation period in expression operations, J. Chem. Eng. Jpn. **7**, 229 (1974).
[31] M. Shirato, T. Murase, N. Hayashi, and T. Fukushima, Constant pressure expression of solid-liquid mixtures with medium resistance, J. Chem. Eng. Jpn. **10**, 154 (1977).
[32] L. Preziosi, D. D. Joseph, and G. S. Beavers, Infiltration of initially dry, deformable porous media, Int. J. Multiphase Flow **22**, 1205 (1996).
[33] X.-S. Yang, Nonlinear viscoelastic compaction in sedimentary basins, Nonlin. Processes Geophys. **7**, 1 (2000).
[34] A. C. Fowler and X.-S. Yang, Loading and unloading of sedimentary basins: The effect of rheological hysteresis, J. Geophys. Res. **107**, ETG–1 (2002).
[35] H. Nanko, D. Hillman, and A. Button, *The World of Market Pulp* (WOMP, Appleton, WI, 2005).
[36] S. Burton and C. Sprague, The instantaneous measurement of density profile development during web consolidation, J. Pulp Paper Sci. **13**, 145 (1987).

[37] J. R. Burns, T. E. Conners, and J. D. Lindsay, Dynamic measurement of density-gradient development during wet pressing, Tappi J. **73**, 107 (1990).
[38] J. Burns, J. Lindsay, and T. Conners, Dynamic measurements of stratified consolidation in a press nip, Tappi J. **76**, 87 (1993).
[39] M. Zytynski, M. F. Randolph, R. Nova, and C. P. Wroth, On modelling the unloading-reloading behaviour of soils, Int. J. Numer. Anal. Methods Geomech. **2**, 87 (1978).
[40] N. Khalili, M. A. Habte, and S. Valliappan, A bounding surface plasticity model for cyclic loading of granular soils, Int. J. Numer. Methods Eng. **63**, 1939 (2005).
[41] M. Mohajerani, P. Delage, M. Monfared, A. M. Tang, J. Sulem, and B. Gatmiri, Oedometric compression and swelling behaviour of the callovo-oxfordian argillite, Int. J. Rock Mech. Mining Sci. **48**, 606 (2011).
[42] T. Wichtmann and T. Triantafyllidis, An experimental database for the development, calibration and verification of constitutive models for sand with focus to cyclic loading: Part I—Tests with monotonic loading and stress cycles, Acta Geotech. **11**, 739 (2016).
[43] B. Simpson, Retaining structures: Displacement and design, Géotechnique **42**, 541 (1992).
[44] A. Niemunis and I. Herle, Hypoplastic model for cohesionless soils with elastic strain range, Mech. Cohes.-Frict. Mater. **2**, 279 (1997).
[45] M. Bode, W. Fellin, D. Mašín, G. Medicus, and A. Ostermann, An intergranular strain concept for material models formulated as rate equations, Int. J. Numer. Anal. Methods Geomech. **44**, 1003 (2020).
[46] Z. Shi and M. Huang, Intergranular-strain elastic model for recent stress history effects on clay, Comput. Geotech. **118**, 103316 (2020).